Liquid Crystalline Order and Magnetocrystalline Anisotropy in Magnetically Doped Semiconducting ZnO Nanowires

Shanju Zhang, Candice I. Pelligra, Gayatri Keskar, Pawel W. Majewski, Fang Ren, Lisa D. Pfefferle, and Chinedum O. Osuji*

Department of Chemical and Environmental Engineering, Yale University, New Haven, Connecticut 06511, United States

ABSTRACT Controlled alignment of nanomaterials over large length scales (>1 cm) presents a challenge in the utilization of low-cost solution processing techniques in emerging nanotechnologies. Here, we report on the lyotropic liquid crystalline behavior of transition-metal-doped zinc oxide nanowires and their facile alignment over large length scales under external fields. High aspect ratio Co- and Mn-doped ZnO nanowires were prepared by solvothermal synthesis with uniform incorporation of dopant ions into the ZnO wurtzite crystal lattice. The resulting nanowires exhibited characteristic paramagnetic behavior. Suspensions of surface-functionalized doped nanowires spontaneously formed stable homogeneous nematic liquid crystalline phases in organic solvent above a critical concentration. Large-area uniaxially aligned thin films of doped nanowires were obtained from the lyotropic phase by applying mechanical shear and, in the case of Co-doped nanowires, magnetic fields. Application of shear produced thin films in which the nanowire long axes were aligned parallel to the flow direction. Conversely, the nanowires were found to orient perpendicular to the direction of the applied magnetic fields. This indicates that the doped ZnO possesses magnetocrystalline anisotropy sufficient in magnitude to overcome the parallel alignment which would be predicted based solely on the anisotropic demagnetizing field associated with the high aspect ratio of the nanowires. We use a combination of magnetic property measurements and basic magnetostatics to provide a lower-bound estimate for the magnetocrystalline anisotropy.

KEYWORDS: nanowires · dilute magnetic semiconductors · lyotropic liquid crystals · magnetic alignment

Recent theoretical advances point to the prospect of room temperature ferromagnetism in III–V and II–VI semiconductors in which a few atomic percent of metal ions are replaced by magnetic transition metal ions such as Mn^{2+} or Co^{2+}.[1−3] Consequently, dilute magnetic semiconductors (DMS) have been a topic of considerable interest in recent years.[4−7] It is worth noting that conflicting reports have been produced in that time, and it is not yet clear under what conditions true high Curie temperature (T_C) DMS materials can be reliably and consistently produced.[8,9] Nonetheless, the ground-breaking potential for spintronic devices utilizing low-cost DMS materials continues to spur work in this field. The ability to simultaneously exploit both electron spin and charge currents makes putative ferromagnetic semiconductors very attractive as a class of materials for the development of new paradigms in computing, both in storage as well as in information processing.[10,11] A particularly exciting area is the development of spintronic devices based on nanowire arrays where structural anisotropy on mesoscopic length scales introduces polarization-dependent optoelectronic properties which are spin-sensitive.[5,12] The use of direct chemical synthesis to controllably produce large gram-scale quantities of nanowires combined with bottom-up assembly by lyotropic ordering in fluid suspensions holds the prospect of the facile realization of such systems. However, to date, such solution-based self-assembly of magnetically doped semiconducting nanowires has not been realized.

We show here that this may be accomplished starting with a simple, optimized solvothermal synthesis to produce high aspect ratio ZnO nanowires with controlled doping by Mn and Co ions. Appropriate functionalization of the nanowire surfaces by thiol ligands successfully suppresses attractive interactions between nanowires, permitting the formation of stable, homogeneous nematic mesophases in organic solvent based only on excluded volume interactions. The nanowires are paramagnetic and display strong alignment under shear flow, resulting in the production of large-area monodomains. We demonstrate that alignment may also be advanced using magnetic field, but only for the case of Co-doped nanowires. Magnetic alignment occurs with the long axes of the nanowires orthogonal to the field direction. This indicates that magnetocrystalline anisotropy

* Address correspondence to chinedum.osuji@yale.edu.

Received for review August 11, 2011 and accepted September 9, 2011.

Published online September 11, 2011
10.1021/nn203070d

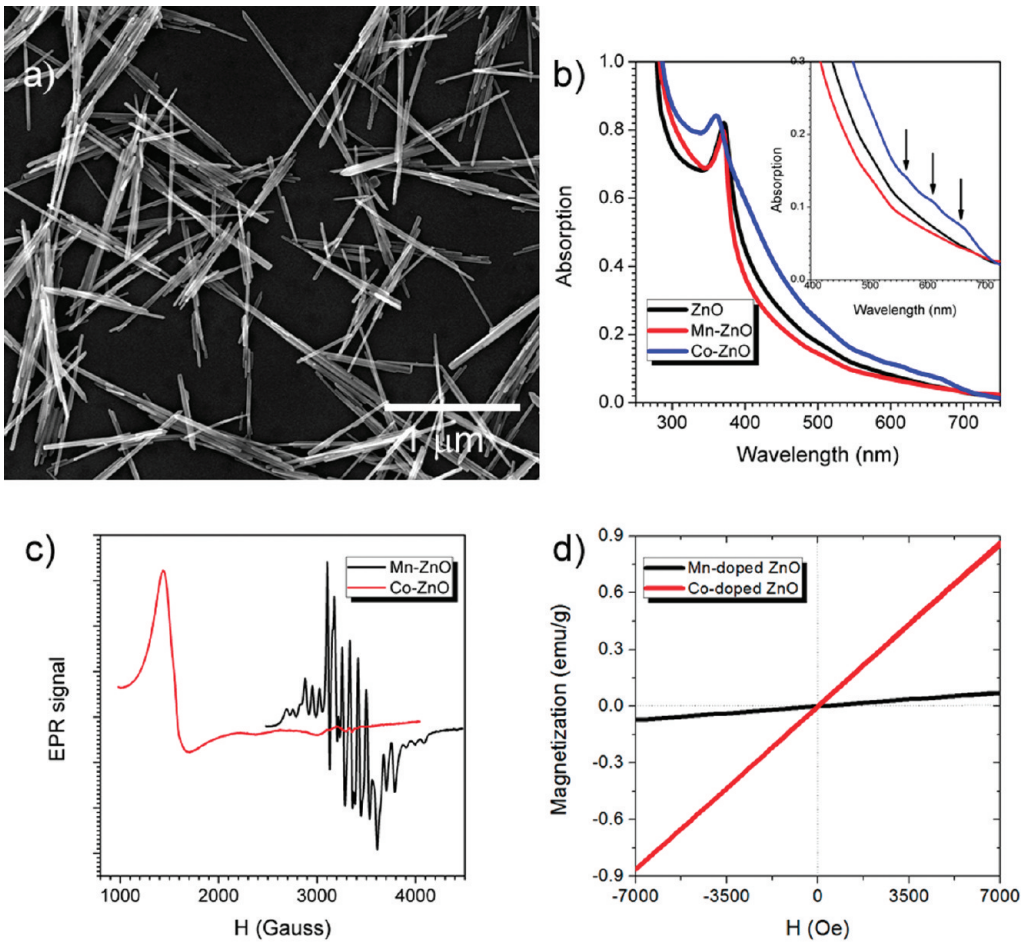

Figure 1. ZnO-based DMS nanowires with 5 atom % Mn and Co dopants. (a) SEM image of Co-doped ZnO nanowires. (b) UV−vis absorption spectra of undoped ZnO and Mn- and Co-doped ZnO nanowires in aqueous solutions. Inset shows the absorption in the visible range. (c) EPR spectra of Mn- and Co-doped ZnO nanowires at room temperature and 7.5 K, respectively. (d) Magnetization *versus* field at 7 K of Mn- and Co-doped ZnO nanowires.

exists in the system and that its effects dominate over shape anisotropy in the field response of these nanowires.

ZnO in its most common wurtzite form is a wide band gap semiconductor with a 3.37 eV direct HOMO−LUMO transition. It forms a hexagonal unit cell in which the absence of inversion symmetry gives rise to both piezoelectric and pyroelectric properties. Both physical deposition techniques and solution-based chemical methods have been developed to synthesize ZnO nanomaterials with a wide variety of morphologies, including nanowires.[13−16] At sufficiently high aspect ratios, anisotropic nanomaterials such as nanowires may undergo a spontaneous ordering transition as a function of volume fraction.[17] Nematic phases are formed as a result of free energy minimization in suspensions of long rigid objects, solely on the basis of entropic or excluded volume interactions. This phenomenon is well-known[18] and entails a transition from an isotropic suspension to a mixture of isotropic and nematic domains for hard rods with no attractive interactions at a volume fraction of $\phi_1^* = 3.34/(L/D)$, where L/D is the aspect ratio of the objects. At $\phi_2^* = 4.49/(L/D)$, the system transitions from a biphasic state to a homogeneous nematic state. Magnetically driven alignment of nematic liquid crystal systems has been well-studied experimentally, including in systems which incorporate second phase materials such as anisotropic gold nanorods,[19] ferromagnetic nanoparticles,[20] and carbon nanotubes.[21] In some cases, the inclusions act as magneto-responsive handles which enhance the alignment of the surrounding nematic. In other cases, the alignment of the nematic by the field is used as a template to control the orientation of nanomaterials. The problem has been well-treated theoretically.[22] Here, by contrast, we describe a system in which the nematogen itself is an anisotropic nanoparticle intrinsically modified for enhanced magnetic anisotropy. We leverage the mobility of the lyotropic phase to produce films of nanomaterials with uniform orientation.

RESULTS AND DISCUSSION

Mn- and Co-doped ZnO nanowires were solvothermally prepared by the reduction of zinc and dopant

ions under basic conditions in anhydrous ethanol under moderate heating. A structure-directing agent was used to guide uniaxial growth. Nanowires were produced with very high selectivity by empirical optimization of the reaction conditions for high-aspect ratio rods with small (<50 nm) diameters. Details are provided in the Supporting Information. The resulting nanowires are polydisperse in length and diameter (Figure 1a) with average aspect ratios of 20 and 12 for Co- and Mn-doped nanowires, respectively. Size distributions are summarized in Figure S1. ZnO is in the commonly observed wurtzite form, and substitutional Co- and Mn-doping has little effect on the hexagonal crystalline structure of the ZnO nanowires as indicated by X-ray diffraction (Figure S2). TEM images show single crystal-like wurtzite lattice structures (Figure S3), similar to the pure ZnO nanowires.[17]

UV−vis absorption spectra recorded from a suspension of freshly prepared nanowires in water show an absorption maximum near 370 nm (Figure 1b), which is in good agreement with the expected band gap of 3.37 eV (368 nm) for ZnO. A small blue shift of the ZnO absorption maximum is observed with Co-doping, consistent with prior reports on Co-doped ZnO.[23] While the spectrum of Mn-doped ZnO nanowires shows no apparent extra absorption in the visible region, the Co-doped ZnO nanowire spectrum shows three absorption peaks at 565, 610, and 665 nm. It has been suggested that these peaks are attributed to d−d absorption levels of the Co^{2+} ions, which are characteristic of Co^{2+} in a tetrahedral crystal field.[24]

Electron paramagnetic resonance (EPR) spectroscopy was used to provide insight regarding the dopant distribution and local environments of dopant ions in the nanowires. The EPR spectrum of Mn-doped ZnO nanowires at room temperature is shown in Figure 1c. In a magnetic field, the spin degeneracy of Mn^{2+} will be lifted by the Zeeman splitting term of the spin Hamiltonian for the ion, resulting in the observation of six energy levels. Hyperfine splitting causes each of these transitions to be split into the characteristic sextuplets exhibited in Figure 1c.[25] The observed hyperfine splitting has a spacing of $\Delta H_{pp} = 75$ G, in good agreement with the bulk value for dilute Mn in ZnO of $\Delta H_{pp} = 76$ G. This indicates an absence of surface state Mn^{2+} ions and shows that the isolated manganese ions are substitutionally incorporated only into the ZnO wurtzite crystal lattice tetrahedral sites.[26] Co-doped samples, on the other hand, did not display any EPR resonance at room temperature. At 7.5 K, the EPR spectrum shows an intense broad resonance at ~1500 G and a weaker band at ~3000 G (Figure 1c). Similar to the appearance of splitting in the Mn-doped nanowire samples, a doublet of peaks with hyperfine splitting into octuplets would be expected in the Co-doped ZnO sample. However, it is typically observed that these signals are substantially broadened by the much stronger

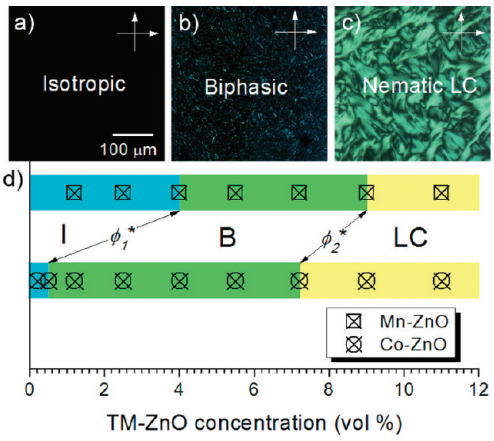

Figure 2. Phase diagram of ZnO-based DMS nanowires in dichlorobenzene. Typical optical images in (a) isotropic, (b) biphasic, and (c) nematic liquid crystalline phases. (d) Phase transitions against concentration. The letters I, B, and LC represent isotropic, biphasic, and liquid crystalline phases, respectively; ϕ_1* and ϕ_2* represent the critical concentrations of biphasic and nematic phase transitions, respectively.

magnetic dipolar interactions of distant Co^{2+} ions in a dilute doped crystal.[27] Comparison with previous studies of materials containing a Co(0) phase further suggests that the broad signals and lack of hyperfine splitting observed at low temperature are consistent with metal cluster-free Co-doped ZnO nanorods.[26] This is supported by X-ray absorption near-edge structure (XANES) spectra (Figure S3 in Supporting Information), which show cobalt ions present only in the Co^{2+} oxidation state, thus ruling out the formation of elemental cobalt phases in the nanowires synthesized here.

Magnetic properties of the doped ZnO nanowires were further examined by superconducting quantum interference device (SQUID) magnetometry. Magnetization curves were recorded as a function of field at 7 K, up to 7 kOe (Figure 1d). Both Mn- and Co-doped samples exhibit purely linear hysteresis-free magnetization, $M(H)$, indicating that no magnetic ordering exists in these materials for temperatures as low as 7 K and that both systems are purely paramagnetic. From the slope of the curves, the magnetic mass susceptibilities, χ_p, are found to be 1.0×10^{-5} and 9.7×10^{-5} cm^3/g for Mn- and Co- doped nanowires, respectively. When an unchanged bulk density relative to ZnO of 5.6 g/cm^3 is assumed, the dimensionless volume susceptibilities are $\chi_m = 7.3 \times 10^{-4}$ and 7.0×10^{-3}. At 5 kOe, the magnetization corresponds to 0.015 and 0.14 μ_B/atom for Mn and Co dopants, respectively, assuming that the nominal transition metal loading of 5 atom % was achieved.

The as-synthesized nanowires have limited dispersibility in liquid media. To study the suspension properties, the nanowires were functionalized by covalent attachment of a short (C_{12}) alkyl chain *via* a thiol end

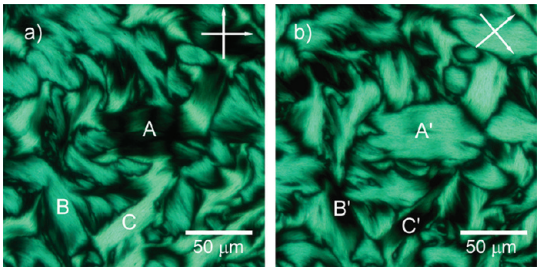

Figure 3. Polarized optical microscopy images of Schlieren textures in the nematic liquid crystalline phase of 11 vol % Co-doped ZnO nanowires in dichlorobenzene. The polydomains become bright and dark as the crossed polarizers rotate. Regions A′, B′, and C′ of the (b) image correspond A, B, and C of the (a) image after 45° rotation of crossed polarizers.

group which reacts with the native ZnO surface.[28−30] Surface functionalization of the nanowires also serves to combat attractive interactions and provides steric repulsions between nanowires, providing conditions closer to the ideal hard-rod interactions described by Onsager theory.[18] It should be noted, however, that liquid crystalline order has also been observed in carbon nanotube suspensions where attractive or "sticky" interactions are very difficult to suppress.[31,32] Momentary sonication of the nanowire/alkyl thiol mixture allowed for uniform functionalization of individual nanowires without the observable presence of aggregates, as probed through mild centrifugation (short ramp over 15 s to 14.5k g-force followed by immediate deceleration). Reaction with the ligand, 1-dodecanethiol (DDT), permits easy dispersal of the nanowires in common organic solvents including chloroform and dichlorobenzene. The resulting dispersion remains homogeneous for weeks without significant visible aggregation under optical microscopy. Figure 2 shows the phase diagram of ZnO-based DMS nanowires in dichlorobenzene. The critical concentration for phase transitions was estimated by examining optical birefringence using polarized light microscopy. Isotropic-to-biphasic and biphasic-to-nematic transitions with increasing concentration were found in both Mn- and Co-doped ZnO nanowire suspensions. In dilute suspensions, the nanowire suspension forms an isotropic phase which appears dark under crossed polarizers. Increasing concentration beyond the critical value ϕ_1* results in biphasic samples which display optically birefringent and thus bright nematic domains distributed in the dark isotropic matrix. Further increasing concentration beyond the critical value ϕ_2* leads to the formation of a single phase with liquid crystalline order. Schlieren textures with black brushes typical of the nematic phase are apparent in the highly concentrated nanowire suspension. Representative optical images of each phase for Mn- and Co-doped ZnO nanowires are also shown in Figures S5 and S6, respectively.

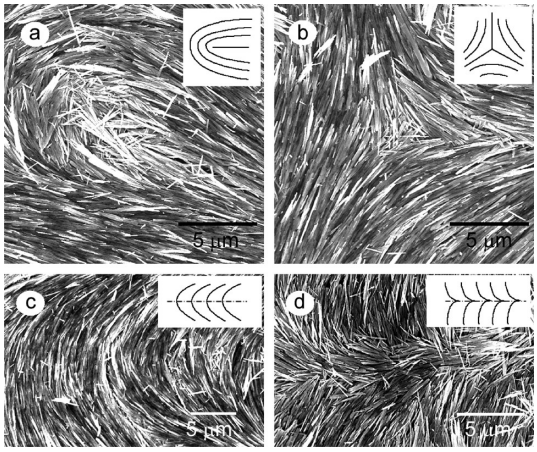

Figure 4. SEM images of Co-doped ZnO nanowires around the liquid crystalline defects: (a) +1/2 disclination, (b) − 1/2 disclination, (c) bend wall, and (d) splay wall. Insets show the corresponding molecular director patterns.

Using polarized optical microscopy, the biphasic range was estimated to be between 3.9 and 9.0 vol % for Mn-doped nanowires and between 0.5 and 7.2 vol % for Co-doped nanowires (Figure 2). Correspondingly, the width of the coexistence regime is 5.1 and 6.7 vol % for Mn- and Co-doped nanowires, respectively. These values are much larger than the theoretical value of 1.2 vol % for monodisperse hard-rod particles.[18] The widening of the biphasic region in both systems is attributed to the substantial polydispersity in the size and aspect ratios of the nanowires and the segregation of longer nanowires to the growing nematic domains. This is especially apparent in the Mn-doped ZnO material which contains a small fraction of low-aspect ratio particles dispersed among the nanowires. A similar widening of the coexistence regime has been observed in polydisperse solutions of tobacco mosaic virus,[33] carbon nanotubes,[34,35] graphene,[36] and inorganic metal and semiconducting nanowires including ZnO[17] and silver nanowires.[37]

Figure 3 shows representative polarized optical microscopy images of ZnO-based DMS nanowires at 11 vol % in dichlorobenzene. The strong birefringence with black brush patterns shows typical Schlieren textures of a polydomain nematic phase.[38] Upon 45° rotation of the crossed polarizers, the dark and bright regions change alternately based on the relative alignment of the nematic director and the polarization vector of the light (Figure 3). A pair of black brushes around a singular point represents a ±1/2 disclination or topological defect. The brushes rotated at twice the angular velocity of the polarizers (Figure S7). Some of the black brushes rotate in the same direction as the crossed polarizers and others in the opposite direction, demonstrating the singularities of strength +1/2 and −1/2, respectively.[39]

The topological defects in lyotropic liquid crystals can be preserved as a thin solid film after the solvent is

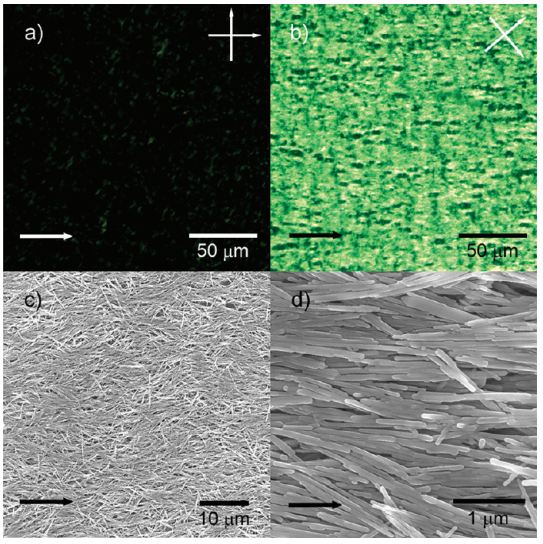

Figure 5. Shear-induced alignment of Co-doped ZnO nanowires in the liquid crystalline phase at 11 vol %. Optical images under crossed polarizers with the shear direction (a) parallel to the polarizer and (b) rotated by 45°. (c) SEM images at low magnification of sheared thin films. (d) SEM image at high magnification of (c). Arrows indicate the shear directions.

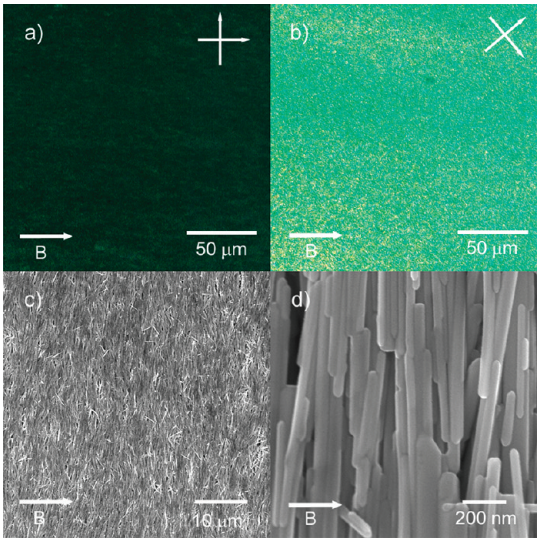

Figure 6. Controlled alignment of 5 wt % Co-doped ZnO nanowires in chloroform suspension during evaporation under a 5 T magnetic field. Arrows indicate the field directions. Optical images under crossed polarizers with the field direction (a) parallel to the polarizer and (b) rotated by 45°. (c) SEM images at low magnification of aligned films. (d) SEM image at high magnification of (c).

completely removed.[40] To demonstrate this, the DMS nanowire organization in the nematic director field was examined by scanning electron microscopy (Figure 4 and Figure S8). Figure 4 shows typical morphologies and structures around isolated topological defects in a dried film. The samples were prepared by solvent evaporation of an 11 vol % nematic liquid crystalline phase on a glass slide. The remaining cooperative organization of individual DMS nanowires is consistent with the director patterns around the disclinations of strengths $s = \pm 1/2$ (Figure 4a,b). It is interesting to note that shorter nanowires with disordered alignments appear to preferentially segregate into the disclination core (Figure 4a,b). The exact reasons for this remain unclear, but we speculate that their decreased ability to form LC phases relative to longer nanowires (at a given volume fraction) leads to a propensity to selectivity reside in the comparatively disordered regions in the vicinity of the disclination cores. Such a disordered structure of the disclination core will reduce the high elastic distortion energies in that region.[41] This observation is consistent with those from experiments conducted on carbon nanotube liquid crystals.[34] Other than $\pm 1/2$ disclinations, the director patterns of isolated inversion walls are also observed (Figure 4c,d). Inversion walls have mirror symmetry and lead to a discontinuous change in the nematic director across the wall. The director undergoes a rotation of π from one side of the wall to the other. It was found that inversion walls connected pairs of adjacent $\pm 1/2$ disclinations (Figure S9), showing analogous behavior of our DMS nanowires to those of ordinary nematic liquid crystals during director reorientation.[42]

Liquid crystalline suspensions of DMS nanowires were readily processed under external fields to produce thin films with large-area microdomains exhibiting a high degree of alignment. Manually applied reciprocating shear between two glass slides at a shear rate of roughly 100 s^{-1} for 2–3 s proved sufficient to produce large-area domains of densely aligned nanowires with long axes aligned parallel to the direction of flow (Figure 5). Optical contrast of the aligned thin film under the crossed polarizers drops to zero when the DMS nanowire axes, serving as the nematic director, are parallel to or perpendicular to the polarizer (at the extinction conditions) (Figure 5a) and is maximized when the axes lie at 45° to the polarizer (Figure 5b). After complete removal of the solvent by evaporation, the thin solid film produced inherits the single-domain nematic order and defect-free alignment of the precursor nematic suspension. SEM images demonstrate that the individual nanowires in the thin film are densely packed and highly aligned along the shear direction (Figure 5c,d).

Magnetic alignment was also investigated by allowing dilute isotropic nanowire suspensions in chloroform to quickly and completely evaporate at 35 °C under a static 5 T field. A large-area monodomain resulted for Co-doped nanowire samples, but only random nanowire arrangements were obtained for Mn-doped materials. We attribute this to the markedly lower magnetic susceptibility of the Mn-doped nanowires. SEM and polarized optical microscopy images of the aligned Co-doped nanowires are shown in Figure 6. The nanowire long axes

are clearly and uniformly oriented perpendicular to the magnetic field, which was vertically applied in the experiment. This clearly rules out alignment by flow patterns due to gravity or drying as the nanowires' long axes are orthogonal to the gravitational field direction, and the resulting monodomain shows no Schlieren structures characteristic of a dried nematic. The driving force for alignment of the system is the minimization of the magnetostatic free energy resulting from the interaction of the external field with the magnetized nanowires. Magnetic energy can be expressed as in eq 1 below where H, the magnetic field strength (or B, the magnetic flux density), has both an internal, or demagnetizing, component and an external component. The demagnetizing component arises from the magnetization of the material itself. The μ_0 is the permeability of free space, a constant, and M is the magnetization of the body by the magnetic field, with $M = \chi H_{ext} = \chi B_{ext}/\mu_0$, where χ is the dimensionless magnetic susceptibility.[43]

$$F = -\frac{1}{2}\mu_0 M \times H_d - \mu_0 M \times H_{ext}$$
$$= -\frac{1}{2} M \times B_d - M \times B_{ext} \quad (1)$$

Alignment due to shape anisotropy originates in the shape-dependent demagnetizing field that exists due to magnetic dipoles on the surface of a body magnetized by an external field. The magnetic field inside the body is given by eq 2, where H_{ext} is the external field and α is the shape factor.

$$H_{int} = H_{ext} - H_d = H_{ext} - \alpha M;$$
$$B_{int} = B_{ext} - B_d = B_{ext} - \alpha M/\mu_0 \quad (2)$$

For a prolate ellipsoid, the demagnetizing field shape factor along the principal axis, α_b, has an asymptotic limit of $(1/r^2)(\log(2r) - 1)$, where r is the aspect ratio of the object.[44] For an infinitely long object, $\alpha_b = 0$ and α_a, the shape factor for the perpendicular orientation is 1/2. Thus, for a magnetically isotropic body with a needle-like shape, alignment with the long axis along the field direction minimizes the free energy.[43] This fact can be used to establish a lower bound for the magnitude of the magnetocrystalline anisotropy in our system. We assume an isotropic, random distribution of Co ions in the lattice with no magnetocrystalline coupling. On this basis, we can estimate the susceptibility of an individual nanowire using the bulk powder measurement obtained through SQUID magnetometry which well represents the stated assumption by measuring a random distribution of cobalt ions in the system. Further assuming that the system behaves as a perfect paramagnet with $\chi \sim 1/T$, we can extrapolate the dimensionless susceptibility to 35 °C, where alignment was conducted to be roughly 2×10^{-4}. For a magnetically isotropic material, the difference in the free energy density due to shape anisotropy, ε (the "self" part of the magnetostatic energy), for infinitely long rods is given by eq 3.[43]

$$\varepsilon = (\chi B)^2/(4\mu_0) \quad (3)$$

From the fact that the system aligns orthogonal to the shape-dictated direction, the magnetocrystalline anisotropy must be of a magnitude sufficient to overcome the shape effects. Thus, $|\Delta\chi| = |\chi_c - \chi_a| > 10^{-8}$ based on the preceding estimates. Since the nanowires align perpendicular to their long axes, we can further deduce that $\chi_a > \chi_c$. This lower limit for the magnetocrystalline anisotropy of our system provides useful insight into shape *versus* crystallinity effects in alignable systems of nanowire arrays. Magnetocrystalline anisotropy with a minimum susceptibility along the *c*-axis has also been observed in Co-doped ZnO films produced by pulsed laser deposition[45−47] but has not, to the knowledge of the authors, been previously demonstrated in single-crystalline, high-aspect ratio DMS nanowires. Such magnetocrystalline anisotropy in dilute doped oxides is indicative of a strong coupling of the orbital moments of the dopant ions to the crystalline field of the oxide. The fact that it is sufficient to overcome shape anisotropy in the system described here is remarkable. Understanding and controlling the interplay between magnetocrystalline anisotropy and shape effects will play important roles in the design of responsive magnetic nanocomposites.

CONCLUSION

In summary, we have demonstrated lyotropic liquid crystalline behavior and bulk alignment of transition-metal-doped zinc oxide nanowires. Dopant ions were uniformly incorporated into zinc sites in the wurtzite crystal lattice without significant phase impurities or clustering, and thus both materials exhibited purely paramagnetic behavior with susceptibilities of 7.3×10^{-4} and 7.0×10^{-3} for Mn- and Co-doped material, respectively. Isotropic-to-liquid crystalline transitions *via* a biphasic region were exhibited for dispersed nanowire systems with increasing concentration, which is characteristic of theoretical predictions for hard-rod particles. Uniaxially aligned thin films of DMS nanowires were then produced by shearing the lyotropic liquid crystalline suspensions followed by drying. Furthermore, uniaxial magnetic alignment of nanowires with their long axis perpendicular to the field was achieved. On the basis of this observation, the influence of magnetocrystalline anisotropy in the system was considered using classical magnetostatics for prolate ellipsoids. The work described here enables fully solution-based processing of liquid crystalline DMS nanowires and a facile route for the fabrication

of macroscopically aligned thin films of these nanowires for emerging applications. Lyotropic self-assembly of nanomaterials is particularly interesting in the context of fabricating magnetic polymer nanocomposites, properties and applications of which have recently been reviewed.[48]

MATERIALS AND METHODS

Synthesis of DMS Nanowires. ZnO-based DMS nanowires were prepared in our own laboratory using solvothermal synthesis. In a typical procedure, metal salts (zinc nitrate or zinc acetate) were dissolved in 150 mL of ethanol to achieve a concentration of 6.67 mM in metal ion with 5 mol % of Co or Mn. Then, 1.2 g of NaOH was added, and the solutions were stirred vigorously for 1 h until turbid. The Co-doped ZnO precursor solution was prepared at atmospheric conditions and was sonicated for 30 min directly after mixing using a Branson Sonifier 450 tip sonicator with a power input of 25 W. The Mn-doped ZnO precursor solution was prepared under nitrogen. Then, 7.5 mL of ethylenediamine (EDA) was added, and the solutions were sonicated for 20 min in a Branson 2510 ultrasonic cleaner. Finally, each solution was transferred to a Teflon linear and sealed in a stainless steel autoclave which was set at 130 °C for 2 days. After naturally cooling to room temperature, the obtained reaction products were collected and purified by washing with water and ethanol. Co-doped nanowires were royal-green in color, and Mn-doped nanowires were light brown in color. For surface modification, 20 mg of DMS nanowires was mixed with 0.202 g of 1-dodecanethiol (DDT) under stirring in chloroform overnight. The resultant products were collected by centrifuge and rinsed with chloroform several times. DDT-modified nanowires were dispersed in dichlorobenzene without any additives. A bulk density of 5.61 g/cm^3 of ZnO was used to convert from a mass to a volume basis.

Characterization of DMS Nanowires. UV−vis absorption spectra of the nanowire suspensions were taken on Cary-100 spectrophotometer at 25 °C. Optical textures of the suspensions were studied in transmission mode under cross polarizers on a Zeiss Axiovert 200 M optical microscope. After solvent complete evaporation, the dried samples were coated by a thin gold layer and examined in a Hitachi SU-70 scanning electron microscope (SEM) with a 10 kV accelerating voltage. Quantitative analysis of nanowire dimensions was performed by imaging a large number of representative nanowires with resolution in either diameter, length, or both dimensions. Images were then analyzed using Image-J software. The X-ray absorption spectra (XAS) data were collected at beamline X23A2 at the National Synchrotron Light Source (NSLS), Brookhaven National Laboratory. The spectra were performed at the Co K edge at 7709 eV at room temperature. Extended X-ray absorption fine structure (EXAFS) spectra were recorded in the transmission mode above the Co K edge. A Co foil reference (4 μm thick) was used to calibrate the edge energy of each scan. A fit of the EXAFS data was performed using the IFEFFIT program based on FEFF 6.0. Perpendicular-mode electron paramagnetic resonance (EPR) spectroscopy was performed at X-band (9.357 GHz) on a Bruker Biospin/ELEXSYS E500 spectrometer equipped with an SHQ cavity and an Oxford ESR900 liquid helium cryostat. Powder samples were sealed in glass tubes purged with N_2 and placed in a 5 mm o.d. quartz EPR tube. For samples collected at cryogenic temperatures, the quartz tube was filled with 40/60 acetone/toluene mixture to stabilize the inner tube and allow efficient heat transfer. All spectra were recorded with microwave power of 1.0 mW. A FEI Tecnai-20 high-resolution transmission electron microscope (HRTEM) was employed to image individual doped nanowires. Two-dimensional wide-angle X-ray diffraction (2-D WAXD) patterns were obtained in a transmission mode on Rigaku 007HF using Rigaku Saturn 944+ CCD detection system. Magnetic properties were measured with a Quantum Design MPMS superconducting quantum interference device (SQUID) magnetometer at temperature of 7 K.

Magnetic Alignment of DMS Nanowires. Magnetic alignment experiments were performed with a superconducting electromagnet designed by American Magnetics Inc. capable of producing a 6 T static field. DDT-functionalized Co-doped ZnO nanowires were dispersed in chloroform to 5 wt % and drop-casted onto piranha-treated hydrophilic silicon wafers. Samples were mounted in a custom sample holder within the vertical bore of the magnet such that the plane of the sample substrate surface was parallel to the direction of the vertical field. The temperature of the sample holder was maintained at 35 °C by enlisting a heating coil and temperature controller. The field was maintained at 5 T until all solvent was completely evaporated from the samples.

Acknowledgment. The authors gratefully acknowledge assistance with EPR measurements from Karin Young and Gary Brudvig as well as the use of Yale facilities supported by MRSEC DMR 0520495 (CRISP). This work was supported by the SOLAR program of the National Science Foundation under DMR-0934520. C.P. acknowledges financial support from the NSF Graduate Research Fellowship Program (GRFP).

Supporting Information Available: Detailed size distribution data, XRD, XANES spectra, TEM images of nanowires, and polarized optical micrographs of nanowire suspensions. This material is available free of charge *via* the Internet at http://pubs.acs.org.

REFERENCES AND NOTES

1. Dietl, T.; Ohno, H.; Matsukura, F.; Cibert, J.; Ferrand, D. Zener Model Description of Ferromagnetism in Zinc-Blende Magnetic Semiconductors. *Science* **2000**, *287*, 1019–1022.
2. Badaeva, E.; Isborn, C. M.; Feng, Y.; Ochsenbein, S. T.; Gamelin, D. R.; Li, X. S. Theoretical Characterization of Electronic Transitions in Co^{2+}- and Mn^{2+}-Doped ZnO Nanocrystals. *J. Phys. Chem. C* **2009**, *113*, 8710–8717.
3. Cheng, S. J. Theory of Magnetism in Diluted Magnetic Semiconductor Nanocrystals. *Phys. Rev. B: Condens. Matter* **2008**, 77.
4. Dietl, T. A Ten-Year Perspective on Dilute Magnetic Semiconductors and Oxides. *Nat. Mater.* **2010**, *9*, 965–974.
5. Kim, U.; Park, T. E.; Kim, I.; Seong, H. K.; Kim, M. H.; Chang, J.; Park, J. G.; Choi, H. J. Magnetic Anisotropy in Vertically Aligned Diluted Magnetic Mn:Ge Semiconductor Nanowires. *J. Appl. Phys.* **2009**, 106.
6. Macdonald, A. H.; Schiffer, P.; Samarth, N. Ferromagnetic Semiconductors: Moving Beyond (Ga, Mn)As. *Nat. Mater.* **2005**, *4*, 195–202.
7. Ogale, S. B. Dilute Doping, Defects, and Ferromagnetism in Metal Oxide Systems. *Adv. Mater.* **2010**, *22*, 3125–3155.
8. Kittilstved, K. R.; Liu, W. K.; Gamelin, D. R. Electronic Structure Origins of Polarity-Dependent High-T-C Ferromagnetismin Oxide-Diluted Magnetic Semiconductors. *Nat. Mater.* **2006**, *5*, 291–297.
9. Alaria, J.; Turek, P.; Bernard, M.; Bouloudenine, M.; Berbadj, A.; Brihi, N.; Schmerber, G.; Colis, S.; Dinia, A. No Ferromagnetism in Mn Doped ZnO Semiconductors. *Chem. Phys. Lett.* **2005**, *415*, 337–341.
10. Wolf, S. A.; Awschalom, D. D.; Buhrman, R. A.; Daughton, J. M.; von Molnar, S.; Roukes, M. L.; Chtchelkanova, A. Y.; Treger, D. M. Spintronics: A Spin-Based Electronics Vision for the Future. *Science* **2001**, *294*, 1488–1495.
11. Beaulac, R.; Archer, P. I.; Ochsenbein, S. T.; Gamelin, D. R. Mn^{2+}-Doped CdSe Quantum Dots: New Inorganic

Materials for Spin-Electronics and Spin-Photonics. *Adv. Funct. Mater.* **2008**, *18*, 3873–3891.
12. Choi, H. J.; Seong, H. K.; Chang, J.; Lee, K. I.; Park, Y. J.; Kim, J. J.; Lee, S. K.; He, R. R.; Kuykendall, T.; Yang, P. D. Single-Crystalline Diluted Magnetic Semiconductor Gan: Mn Nanowires. *Adv. Mater.* **2005**, *17*, 1351–1356.
13. Wei, Y. G.; Wu, W. Z.; Guo, R.; Yuan, D. J.; Das, S. M.; Wang, Z. L. Wafer-Scale High-Throughput Ordered Growth of Vertically Aligned ZnO Nanowire Arrays. *Nano Lett.* **2010**, *10*, 3414–3419.
14. Greene, L. E.; Law, M.; Goldberger, J.; Kim, F.; Johnson, J. C.; Zhang, Y. F.; Saykally, R. J.; Yang, P. D. Low-Temperature Wafer-Scale Production of ZnO Nanowire Arrays. *Angew. Chem., Int. Ed.* **2003**, *42*, 3031–3034.
15. Liu, B.; Zeng, H. C. Room Temperature Solution Synthesis of Monodispersed Single-Crystalline ZnO Nanorods and Derived Hierarchical Nanostructures. *Langmuir* **2004**, *20*, 4196–4204.
16. Wang, Z. L. ZnO Nanowire and Nanobelt Platform for Nanotechnology. *Mater. Sci. Eng., R* **2009**, *64*, 33–71.
17. Zhang, S. J.; Majewski, P. W.; Keskar, G.; Pfefferle, L. D.; Osuji, C. O. Lyotropic Self-Assembly of High-Aspect-Ratio Semiconductor Nanowires of Single-Crystal ZnO. *Langmuir* **2011**, *27*, 11616–11621.
18. Onsager, L. The Effects of Shape on the Interaction of Colloidal Particles. *Ann. N.Y. Acad. Sci.* **1949**, *51*, 627–659.
19. Liu, Q.; Cui, Y.; Gardner, D.; Li, X.; He, S.; Smalyukh, I. I. Self-Alignment of Plasmonic Gold Nanorods in Reconfigurable Anisotropic Fluids for Tunable Bulk Metamaterial Applications. *Nano Lett.* **2010**, *10*, 1347–1353.
20. Vallooran, J. J.; Bolisetty, S.; Mezzenga, R. Macroscopic Alignment of Lyotropic Liquid Crystals Using Magnetic Nanoparticles. *Adv. Mater.* **2011**, 3932–3937.
21. Buluy, O.; Nepijko, S.; Reshetnyak, V.; Ouskova, E.; Zadorozhnii, V.; Leonhardt, A.; Ritschel, M.; Schonhense, G.; Reznikov, Y. Magnetic Sensitivity of a Dispersion of Aggregated Ferromagnetic Carbon Nanotubes in Liquid Crystals. *Soft Matter* **2011**, *7*, 644–649.
22. Brochard, F.; de Gennes, P. G. Theory of Magnetic Suspensions in Liquid Crystals. *J. Phys.* **1970**, *31*, 691–708.
23. Yang, Y. F.; Jin, Y. Z.; He, H. P.; Wang, Q. L.; Tu, Y.; Lu, H. M.; Ye, Z. Z. Dopant-Induced Shape Evolution of Colloidal Nanocrystals: The Case of Zinc Oxide. *J. Am. Chem. Soc.* **2010**, *132*, 13381–13394.
24. Bilecka, I.; Luo, L.; Djerdj, I.; Rossell, M. D.; Jagodic, M.; Jaglicic, Z.; Masubuchi, Y.; Kikkawa, S.; Niederberger, M. Microwave-Assisted Nonaqueous Sol−Gel Chemistry for Highly Concentrated ZnO-Based Magnetic Semiconductor Nanocrystals. *J. Phys. Chem. C* **2011**, *115*, 1484–1495.
25. Diaconu, M.; Schmidt, H.; Poppl, A.; Bottcher, R.; Hoentsch, J.; Klunker, A.; Spemann, D.; Hochmuth, H.; Lorenz, M.; Grundmann, M. Electron Paramagnetic Resonance of Zn1-Xmnxo Thin Films and Single Crystals. *Phys. Rev. B: Condens. Matter* **2005**, 72.
26. Clavel, G.; Willinger, M. G.; Zitoun, D.; Pinna, N. Solvent Dependent Shape and Magnetic Properties of Doped ZnO Nanostructures. *Adv. Funct. Mater.* **2007**, *17*, 3159–3169.
27. Azamat, D. V.; Dejneka, A.; Trepakov, V. A.; Jastrabik, L.; Fanciulli, M.; Ivanov, V. Y.; Godlewski, M.; Sokolov, V. I.; Rosa, J.; Badalyan, A. G. EPR Spectroscopy of Weak Exchange Interactions between Co^{2+} Ions in ZnO. *Phys. Status Solidi RRL* **2011**, *5*, 138–140.
28. Singh, J.; Im, J.; Whitten, J. E.; Soares, J. W.; Steeves, D. M. Encapsulation of Zinc Oxide Nanorods and Nanoparticles. *Langmuir* **2009**, *25*, 9947–9953.
29. Deng, S. Z.; Fan, H. M.; Wang, M.; Zheng, M. R.; Yi, J. B.; Wu, R. Q.; Tan, H. R.; Sow, C. H.; Ding, J.; Feng, Y. P.; *et al.* Thiol-Capped ZnO Nanowire/Nanotube Arrays with Tunable Magnetic Properties at Room Temperature. *ACS Nano* **2010**, *4*, 495–505.
30. Sadik, P. W.; Pearton, S. J.; Norton, D. P.; Lambers, E.; Ren, F. Functionalizing Zn- and O-Terminated ZnO with Thiols. *J. Appl. Phys.* **2007**, 101.
31. Hobbie, E. K.; Fry, D. J. Nonequilibrium Phase Diagram of Sticky Nanotube Suspensions. *Phys. Rev. Lett.* **2006**, *97*, 036101.
32. Lu, L.; Chen, W. Large-Scale Aligned Carbon Nanotubes from Their Purified, Highly Concentrated Suspension. *ACS Nano* **2010**, *4*, 1042–1048.
33. Oster, G. 2-Phase Formation in Solutions of Tobacco Mosaic Virus and the Problem of Long-Range Forces. *J. Gen. Physiol.* **1950**, *33*, 445–473.
34. Zhang, S. J.; Kinloch, I. A.; Windle, A. H. Mesogenicity Drives Fractionation in Lyotropic Aqueous Suspensions of Multiwall Carbon Nanotubes. *Nano Lett.* **2006**, *6*, 568–572.
35. Davis, V. A.; Parra-Vasquez, A. N. G.; Green, M. J.; Rai, P. K.; Behabtu, N.; Prieto, V.; Booker, R. D.; Schmidt, J.; Kesselman, E.; Zhou, W.; *et al.* True Solutions of Single-Walled Carbon Nanotubes for Assembly into Macroscopic Materials. *Nat. Nanotechnol.* **2009**, *4*, 830–834.
36. Behabtu, N.; Lomeda, J. R.; Green, M. J.; Higginbotham, A. L.; Sinitskii, A.; Kosynkin, D. V.; Tsentalovich, D.; Parra-Vasquez, N. G.; Schmidt, J.; Kesselman, E.; *et al.* Spontaneous High-Concentration Dispersions and Liquid Crystals of Graphene. *Nat. Nanotechnol.* **2010**, *5*, 406–411.
37. Murali, S.; Xu, T.; Marshall, B. D.; Kayatin, M. J.; Pizarro, K.; Radhakrishnan, V. K.; Nepal, D.; Davis, V. A. Lyotropic Liquid Crystalline Self-Assembly in Dispersions of Silver Nanowires and Nanoparticles. *Langmuir* **2010**, *26*, 11176–11183.
38. Zhang, S. J.; Li, Q. W.; Kinloch, I. A.; Windle, A. H. Ordering in a Droplet of an Aqueous Suspension of Single-Wall Carbon Nanotubes on a Solid Substrate. *Langmuir* **2010**, *26*, 2107–2112.
39. Kim, J. E.; Han, T. H.; Lee, S. H.; Kim, J. Y.; Ahn, C. W.; Yun, J. M.; Kim, S. O. Graphene Oxide Liquid Crystals. *Angew. Chem., Int. Ed.* **2011**, *50*, 3043–3047.
40. Song, W. H.; Kinloch, I. A.; Windle, A. H. Nematic Liquid Crystallinity of Multiwall Carbon Nanotubes. *Science* **2003**, *302*, 1363–1363.
41. Zhang, S. J.; Terentjev, E. M.; Donald, A. M. Nature of Disclination Cores in Liquid Crystals. *Liq. Cryst.* **2005**, *32*, 69–75.
42. Zhang, S. J.; Terentjev, E. M.; Donald, A. M. Disclinations and Their Interactions in Thin Films of Side-Chain Liquid Crystalline Polymers. *Macromolecules* **2004**, *37*, 390–396.
43. Furlani, E. P. *Permanent Magnet and Electromechanical Devices: Materials, Analysis, and Applications*, 1st ed.; Academic Press: San Diego, CA, 2001; p 518.
44. Schenck, J. F. The Role of Magnetic Susceptibility in Magnetic Resonance Imaging: MRI Magnetic Compatibility of the First and Second Kinds. *Med. Phys.* **1996**, *23*, 815–850.
45. Deng, J. X.; Tian, Y. F.; He, S. M.; Bai, H. L.; Xu, T. S.; Yan, S. S.; Dai, Y. Y.; Chen, Y. X.; Liu, G. L.; Mei, L. M. Strong Anisotropy of Magnetization and Sign Reversion of Ordinary Hall Coefficient in Single Crystal $Ge_{1-x}Mn_x$ Magnetic Semiconductor Films. *Appl. Phys. Lett.* **2009**, 95.
46. Subramanian, M.; Tanemura, M.; Hihara, T.; Ganesan, V.; Soga, T.; Jimbo, T. Magnetic Anisotropy in Nanocrystalline Co-Doped ZnO Thin Films. *Chem. Phys. Lett.* **2010**, *487*, 97–100.
47. Venkatesan, M.; Fitzgerald, C. B.; Lunney, J. G.; Coey, J. M. D. Anisotropic Ferromagnetism in Substituted Zinc Oxide. *Phys. Rev. Lett.* **2004**, 93.
48. Dai, Q.; Nelson, A. Magnetically-Responsive Self Assembled Composites. *Chem. Soc. Rev.* **2010**, *39*, 4057–4066.